Cao *et al. Particle and Fibre Toxicology* (2025) 22:1
https://doi.org/10.1186/s12989-024-00616-3

Particle and Fibre Toxicology

RESEARCH Open Access

Deciphering key nano-bio interface descriptors to predict nanoparticle-induced lung fibrosis

Jiayu Cao[1†], Yuhui Yang[1†], Xi Liu[2], Yang Huang[3], Qianqian Xie[2], Aliaksei Kadushkin[4], Mikhail Nedelko[5], Di Wu[2], Noel J. Aquilina[6], Xuehua Li[3], Xiaoming Cai[1*] and Ruibin Li[2,7*]

Abstract

Background The advancement of nanotechnology underscores the imperative need for establishing in silico predictive models to assess safety, particularly in the context of chronic respiratory afflictions such as lung fibrosis, a pathogenic transformation that is irreversible. While the compilation of predictive descriptors is pivotal for in silico model development, key features specifically tailored for predicting lung fibrosis remain elusive. This study aimed to uncover the essential predictive descriptors governing nanoparticle-induced pulmonary fibrosis.

Methods We conducted a comprehensive analysis of the trajectory of metal oxide nanoparticles (MeONPs) within pulmonary systems. Two biological media (simulated lung fluid and phagolysosomal simulated fluid) and two cell lines (macrophages and epithelial cells) were meticulously chosen to scrutinize MeONP behaviors. Their interactions with MeONPs, also referred to as nano-bio interactions, can lead to alterations in the properties of the MeONPs as well as specific cellular responses. Physicochemical properties of MeONPs were assessed in biological media. The impact of MeONPs on cell membranes, lysosomes, mitochondria, and cytoplasmic components was evaluated using fluorescent probes, colorimetric enzyme substrates, and ELISA. The fibrogenic potential of MeONPs in mouse lungs was assessed by examining collagen deposition and growth factor release. Random forest classification was employed for analyzing in chemico, in vitro and in vivo data to identify predictive descriptors.

Results The nano-bio interactions induced diverse changes in the 4 characteristics of MeONPs and had variable effects on the 14 cellular functions, which were quantitatively evaluated in chemico and in vitro. Among these 18 quantitative features, seven features were found to play key roles in predicting the pro-fibrogenic potential of MeONPs. Notably, IL-1β was identified as the most important feature, contributing 27.8% to the model's prediction. Mitochondrial activity (specifically NADH levels) in macrophages followed closely with a contribution of 17.6%. The remaining five key features include TGF-β1 release and NADH levels in epithelial cells, dissolution in lysosomal simulated fluids, zeta potential, and the hydrodynamic size of MeONPs.

†Jiayu Cao and Yuhui Yang are contributed equally to this work.

*Correspondence:
Xiaoming Cai
xmcai@suda.edu.cn
Ruibin Li
liruibin@suda.edu.cn

Full list of author information is available at the end of the article

Conclusions The pro-fibrogenic potential of MeONPs can be predicted by combination of key features at nano-bio interfaces, simulating their behavior and interactions within the lung environment. Among the 18 quantitative features, a combination of seven in chemico and in vitro descriptors could be leveraged to predict lung fibrosis in animals. Our findings offer crucial insights for developing in silico predictive models for nano-induced pulmonary fibrosis.

Keywords lung fibrosis, predictive toxicology, nanosafety, nanotoxicity, biotransformation

Introduction

Nowadays, nano-enabled products have gained widespread utilization across various industries, including cosmetics [1], foods [2, 3], pharmaceuticals [4], electronics [5], automotives [6] and building materials [7]. According to the Nanotechnology Products Database, there are approximately 11,000 nanoproducts in the market, with 4,395 of them specifying the chemical formula of nanomaterial used [8]. Among these, around 12.6% contains metal oxide nanoparticles (MeONPs). Throughout the life cycle of nanoproducts, the release of engineered nanomaterials (ENMs) into the environment poses potential health implications. Humans can be exposed to ENMs through various routes, including inhalation, ingestion, dermal contact, and injection routes [9]. Of these, considerable safety concerns have arisen specifically from inhalation exposure to engineered nanomaterials (ENMs), particularly those used in printing, medicine, cosmetics, and textiles. In the medical field, products such as respiratory masks, disinfecting sprays, anti-bacterial sprays, lung surfactants, wound rinsing sprays, and burn rinsing sprays may release NPs that pose inhalation risks to consumers. Similarly, in cosmetics, skin and hair spray products may also release particles and cause inhalation exposure during use. Inhaled NPs have been found to induce a variety of adverse effects, including respiratory disease [10], systemic inflammation [11], cardiovascular disease [12], reproductive disorder [13], neurological disorder [14], and cancer [15]. Especially, numerous studies have explored the potential link between exposure to ENMs and the onset of chronic respiratory diseases. For instance, occupational studies have shown that inhaled aluminum oxide (Al_2O_3) particles are linked to pulmonary fibrosis, asthma, chronic obstructive lung diseases and possibly lung cancer [16–20]. In addition, many rodent inhalation studies have indicated potential associations between respiratory exposure to MeONPs such as zinc oxide (ZnO) [21, 22], cerium dioxide (CeO_2) [23, 24], and titanium dioxide (TiO_2) [25] and pulmonary fibrosis. The detrimental effects of ENMs may potentially impact the progress of nanotechnology. For instance, scientists speculate that the inclusion of carbon nanotubes in regulatory list of SIN ('Substitute It Now') [26] may discourage research and investment in these materials [27]. Given the exponential rise in nanoproducts, the efficient assessment of nanoparticle-induced chronic respiratory injuries assumes paramount importance for the sustainable advancement of nanotechnology.

The computational (in silico) predictive methods have emerged as valuable approaches for the rapid assessment of nanosafety, offering advantages such as reduced time, labor, and animal costs compared to conventional experimental methods [28, 29]. The successful development of in silico models often relies on the identification of predictive descriptors [29], which often need cell or animal experiments to acquire sufficient data for the model training or testing. For instance, considering that quantum dot (QD)-induced cell deaths are often attributed to surface chemistry factors such as size, ligand, and surface shell, Oh et al. successfully crafted predictive cytotoxicity models for cell viability and IC50 assessments [30]. Furthermore, the identification of NLRP3 inflammasome activation and IL-1β release in the interactions between MeONP and alveolar macrophages (31, 32) has significantly contributed to the formulation of in silico predictive models for MeONP-induced acute lung inflammation [33]. These in silico models markedly accelerate the assessment of acute nanotoxicity. Given that nanoparticle-induced chronic respiratory injuries, such as lung fibrosis, entail an irreversible pathogenic transformation, the demand for in silico predictive models specific to nanoparticle-induced lung fibrosis is pressing. However, the lack of reliable predictive features for lung fibrosis hampers the establishment of in silico models, primarily because nanoparticle-induced lung fibrosis involves intricate nano-bio interactions that cannot be comprehensively mirrored at a singular nano-bio interface. Taking MeONP-induced lung fibrosis as an example, inhaled MeONPs traverse lung lining fluids and accumulate in lung alveoli, where they may internalized by macrophages or epithelial cells, engaging with subcellular organelles such as membranes, lysosomes, mitochondria, etc [34]. Profibrogenic effects may result from cellular damage caused by metal ions or MeONPs and from persistent inflammation induced by long-retained MeONPs. All these events collectively contribute to the onset of pulmonary fibrosis. Our hypothesis posits that predictive descriptors for lung fibrosis can be discerned through a comprehensive analysis of features throughout the entire biological fate of MeONPs.

In this study, our objective was to pinpoint the predictive features implicated in MeONP-induced lung fibrosis. To achieve this goal, we embarked on a comprehensive exploration of the biological fate of MeONPs within the lungs. Constructing a library encompassing 50 distinct MeONPs, we systematically scrutinized their interactions across various biological milieus, including lung lining fluids, plasma membranes, lysosomes, mitochondria, and other cytoplasmic components. Through the collection of quantitative features at these diverse interfaces, our aim was to discern the pivotal factors contributing to MeONP-induced lung fibrosis. Simultaneously, we examined the fibrogenic potential of the MeONPs through collagen staining and the measurement of TGF-β1 production. The quantitative features acquired in chemico and in vitro were subsequently subjected to analysis alongside two fibrogenic indexes determined in vivo. This holistic approach empowered us to identify seven critical descriptors intricately linked to the development of lung fibrosis. Collectively, our study represents the first report of a descriptor formula to predict MeONP-induced lung fibrosis.

Results

Visualization of MeONP distribution in the lungs

For an in-depth exploration of the biological trajectory of MeONPs within the lungs, La_2O_3 was selected as a representative MeONP, and its dynamics were investigated using radioactive iodine (^{125}I) labeling (Figure S1). This assessment aimed to determine whether MeONPs exhibited prolonged retention in the lungs, potentially facilitating extended interaction with pulmonary cells. Single-photon emission computed tomography/computed tomography (SPECT/CT) was employed to trace the biodistribution of ^{125}I-labeled MeONPs in mouse lungs following intratracheal aspiration. As illustrated in Figure S1, ^{125}I-labeled NPs exhibited a significant accumulation in lung tissues post-exposure, demonstrating a gradual, time-dependent clearance from the lungs. Notably, even after 18 days, La_2O_3 showcased a considerable retention (11.69%) in mouse lungs. To gain deeper insights, lung tissues collected at 16 h post-exposure were fixed and stained to prepare sections for observation through transmission electron microscopy (TEM). Significantly, MeONPs were predominantly localized in the alveoli or internalized by macrophages/epithelial cells in proximity to the air-blood barrier (Fig. 1A). Upon magnification of the La_2O_3-rich regions within cells, a distinct distribution in lysosomes was evident. In a concurrent exploration of the intracellular trajectory of La_2O_3, a macrophage-like cell line, THP-1 cells, was exposed to fluorescein isothiocyanate (FITC)-labeled La_2O_3, emitting intense fluorescence at 490 nm. As depicted in Fig. 1B, FITC-La_2O_3 exhibited a time-dependent distribution pattern, including association with cytoplasmic membranes at 0–4 h, lysosomal internalization at 6–12 h, and subsequent release into the cytoplasm after 24 h.

Interactions between MeONPs and biological fluids

According to the trajectory of MeONPs within the lungs, the particles engage with two distinct biological fluids within alveoli and lysosomes. An assortment of 50 MeONPs (Table S1) underwent scrutiny to discern their interactions in simulated lung fluid (SLF) and phagolysosomal simulated fluid (PSF), encompassing assessments of hydrodynamic size, surface charge, and dissolution rate (Fig. 2). In SLF, all MeONPs were noted to aggregate with a significant increase in size, exhibiting hydrodynamic sizes ranging from 143 to 2515 nm. Among these particles, twenty MeONPs, including TiO_2-3, CuO-1, CuO-2, Fe_2O_3-1, Fe_2O_3-2, MnO_2-2, Co_3O_4-1, Co_3O_4-2, Cr_2O_3, MoO_3, SnO_2, Sb_2O_3, Eu_2O_3-2, Nd_2O_3, Sm_2O_3, Pr_2O_3, Tb_2O_3, Tm_2O_3, Ho_2O_3,and Er_2O_3, exhibited negative surface charges with Zeta potentials ranging from −1.72 to -29.50 mV, while other MeONPs demonstrated positive Zeta potentials ranging from 0.10 to 42.60 mV. Moreover, we investigated the dissolution of MeONPs in the two biological fluids. In SLF, all MeONPs exhibited low dissolution (<2%), whereas 11 MeONPs (Al_2O_3-1, CuO-1, CuO-2, ZnO-1, ZnO-2, ZnO-3, MoO_3, MgO, Sb_2O_3, Eu_2O_3-1, La_2O_3) demonstrated elevated dissolution rates (10-70%) in PSF. In addition, we calculated the dosimetry of all MeONPs in two cell culture media for THP-1 and BEAS-2B cells in 96-well plates using the ISDD model [35] (Table S2).

Impacts of MeONPs on cellular functions

Based on the intracellular trajectory of La_2O_3, we assessed the impacts of MeONPs on lung cells by examining various cellular parameters, including plasma membrane integrity, lysosomal pH changes, mitochondria metabolic activity, oxidative stress generation, and cytokine production. These features were normalized by comparing them with control (0 μg/ml) cells and presented in heatmaps (Fig. 3 and Figure S2) or histogram (Fig. 4 and S3).

Plasma membrane integrity of THP-1 and BEAS-2B cells was determined by detecting lactate dehydrogenase (LDH) release into the supernatants. As illustrated in Fig. 3, CuO-1, CuO-2, and ZnO-1 induced>50% LDH leakage from THP-1 cells at 200 μg/ml. Seventeen MeONPs (TiO_2-1, α-MnO_2, Co_3O_4-2, Co_3O_4-3, etc.) caused moderate membrane damage (20–50% LDH release), while the remaining 30 MeONPs had limited effects on membrane integrity. In contrast, MeONPs exhibited different effects on BEAS-2B cell membranes. Overall, BEAS-2B cells were less sensitive to

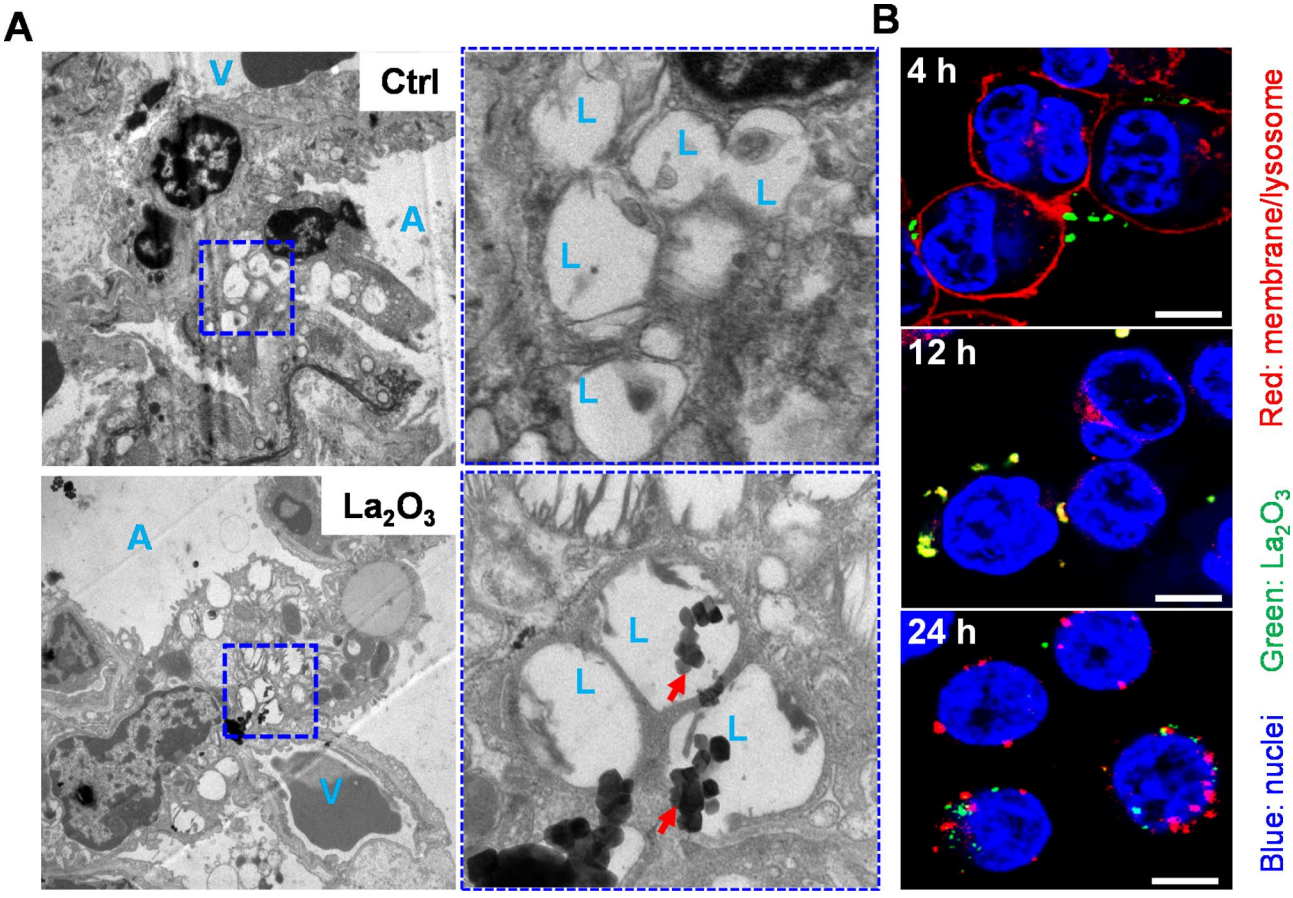

Fig. 1 Visualization of a representative MeONP, La_2O_3, in mouse lungs
(A) TEM imaging of MeONPs in lung tissues. Mice exposed to La_2O_3 were sacrificed at 24 h, and lung tissue sections were prepared for TEM observations. Arrows, A, V, and L indicate MeONP, alveoli, vessels, and lysosomes, respectively, in TEM images. **(B)** Confocal imaging of MeONPs in cells. THP-1 cells exposed to 50 μg/mL FITC-labeled MeONPs were fixed and stained with Hoechst 33,342 (blue), WGA conjugated with Alexa Fluor 594 (red), or LysoTracker DND-99DAPI (red) for confocal imaging

MeONP-induced plasma membrane damage than THP-1 cells. Only two MeONPs (Nd_2O_3, MnO_2-1) evoked 72–75% LDH release from BEAS-2B cells, while four MeONPs (TiO_2-5, MnO_2-2, MgO, and Tb_2O_3) showed moderate effects with 21–45% LDH release (Figure S2).

Lysosomal pH changes were assessed using the pH-sensitive sensor pHLys Red, which accumulates in intact lysosomes and emits red fluorescence in acidic conditions. Surprisingly, CeO_2-2, CeO_2-3, Eu_2O_3-2, La_2O_3, Tb_2O_3, and Ho_2O_3 induced lysosomal acidity, whereas most MeONPs, particularly CuO-1 and Fe_2O_3-3, led to lysosomal alkalization (Fig. 3).

Mitochondrial activity was examined by detecting nicotinamide adenine dinucleotide hydride (NADH) content and ATP levels. Eleven MeONPs, including CuO-1, CuO-2, MnO_2-1, MnO_2-2, ZnO-1, ZnO-2, ZnO-3, Cr_2O_3, CeO_2-3, Eu_2O_3-1 and Dy_2O_3, induced dose-dependent NADH decrease in both THP-1 and BEAS-2B cells (Fig. 3 and Figure S2). Three MeONPs, i.e. Co_3O_4-1, Co_3O_4-2, and Co_3O_4-3, caused NADH decrease only in THP-1 cells, while 12 MeONPs (TiO_2-2, TiO_2-5, Fe_2O_3-2, Bi_2O_3, Y_2O_3, etc.) affected NADH content in BEAS-2B cells. The effects on ATP production mirrored those on NADH, except for Fe_2O_3-1, Eu_2O_3-2, Tb_2O_3, and Ho_2O_3, which showed negligible effects on NADH in THP-1 cells but significantly affected ATP production.

MeONP-induced ROS generation was visualized using the fluorogenic probe 2', 7'-dichlorodihydrofluorescein diacetate (DCFH-DA), with its oxidation form (DCF) emitting strong fluorescence at 520 nm. While most MeONPs had a negligible effect on biological redox homeostasis with limited ROS generation in THP-1 cells (Figs. 3), 11 MeONPs (TiO_2-1, TiO_2-2, TiO_2-3, TiO_2-4, TiO_2-5, MnO_2-1, MnO_2-2, etc.) induced significantly higher cellular ROS levels in BEAS-2B cells, at least 2 times higher than that in the control (Figure S2).

We also measured pro-inflammatory cytokines (TNF-α, IL-1β, IL-6, MCP-1) in THP-1 cells and the growth factor (TGF-β1) in BEAS-2B cells (Table S3 and S4). Among them, IL-1β was the most affected cytokine (Fig. 4).

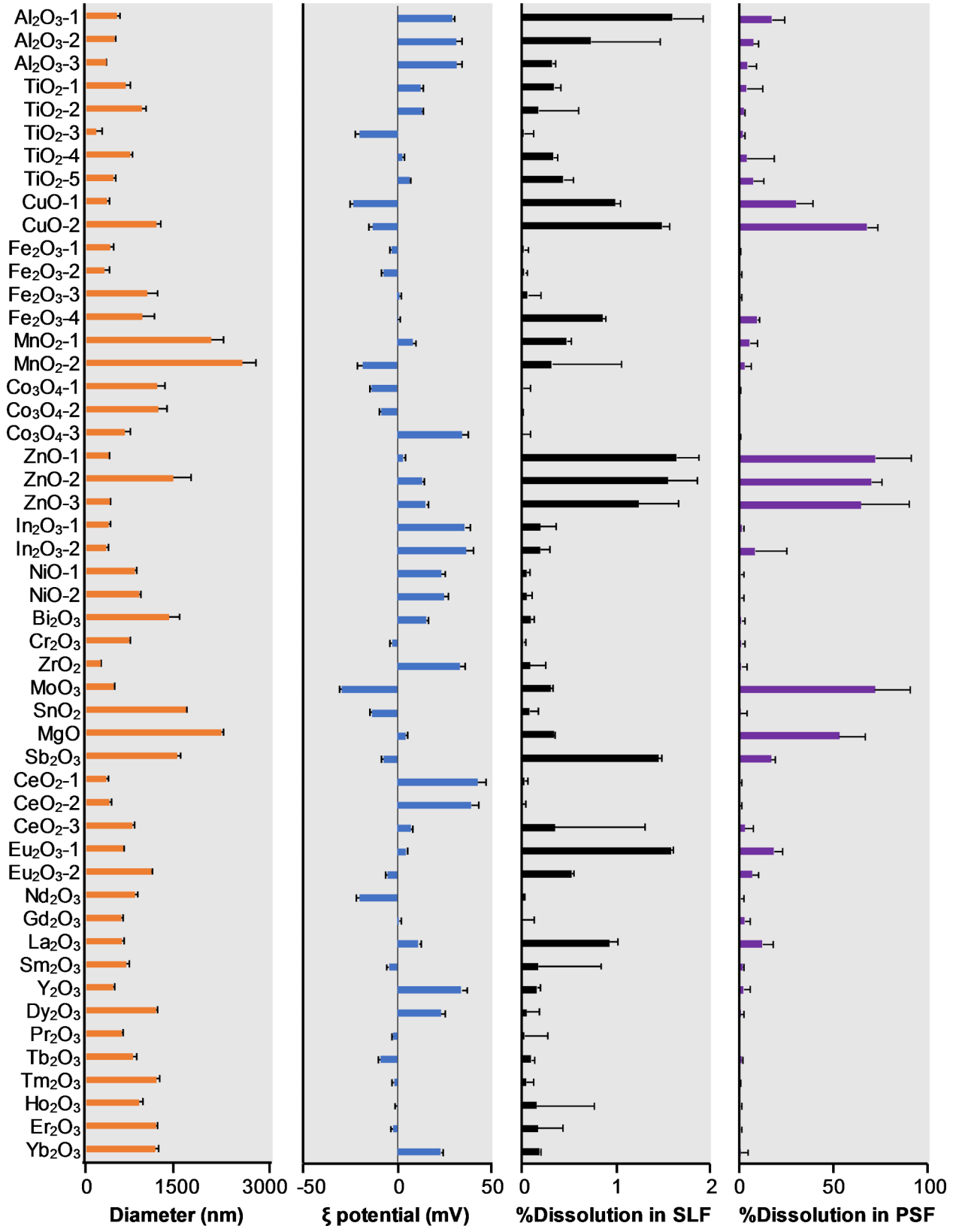

Fig. 2 The hydrodynamic size, surface charge, and dissolution rate of MeONPs
MeONPs were dispersed in SLF or PSF at 50 μg/mL. The hydrodynamic diameters and surface charges of MeONP dispersions were determined by dynamic light scattering and zeta potential analyzer, respectively. The supernatants of MeONP dispersions were collected after 24 h of incubation to detect metal ions by ICP-OES and calculate dissolution rates. Results were calculated from three replicates

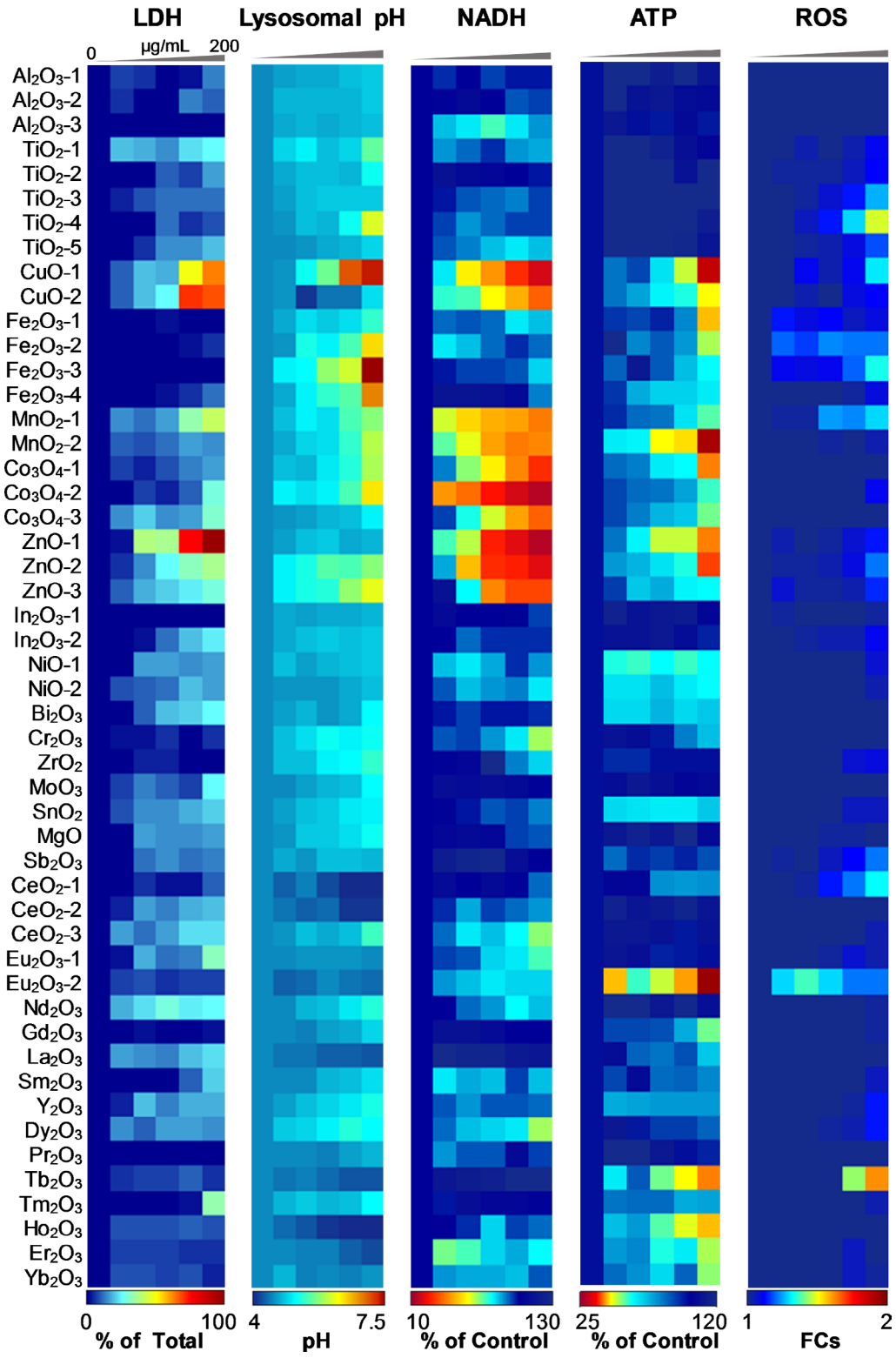

Fig. 3 Heatmap displaying the impacts of MeONPs on THP-1 cells
THP-1 cells were exposed to 0, 12.5, 25, 50, 100, and 200 μg/mL MeONPs for 24 h, followed by LDH measurement in supernatants and lysosomal pH, NADH, ATP, ROS detection in cells. The resulting values of LDH were expressed as percentage (%) of total LDH in THP-1 cells (determined for each experiment by measuring the supernatant of sister cultures after 24 h of exposure to 2% Triton X-100), while the NADH and ATP were expressed as percentage (%) of the control cells. ROS were expressed by the fold changes (FCs) of measured values in MeONP treatments and control cells

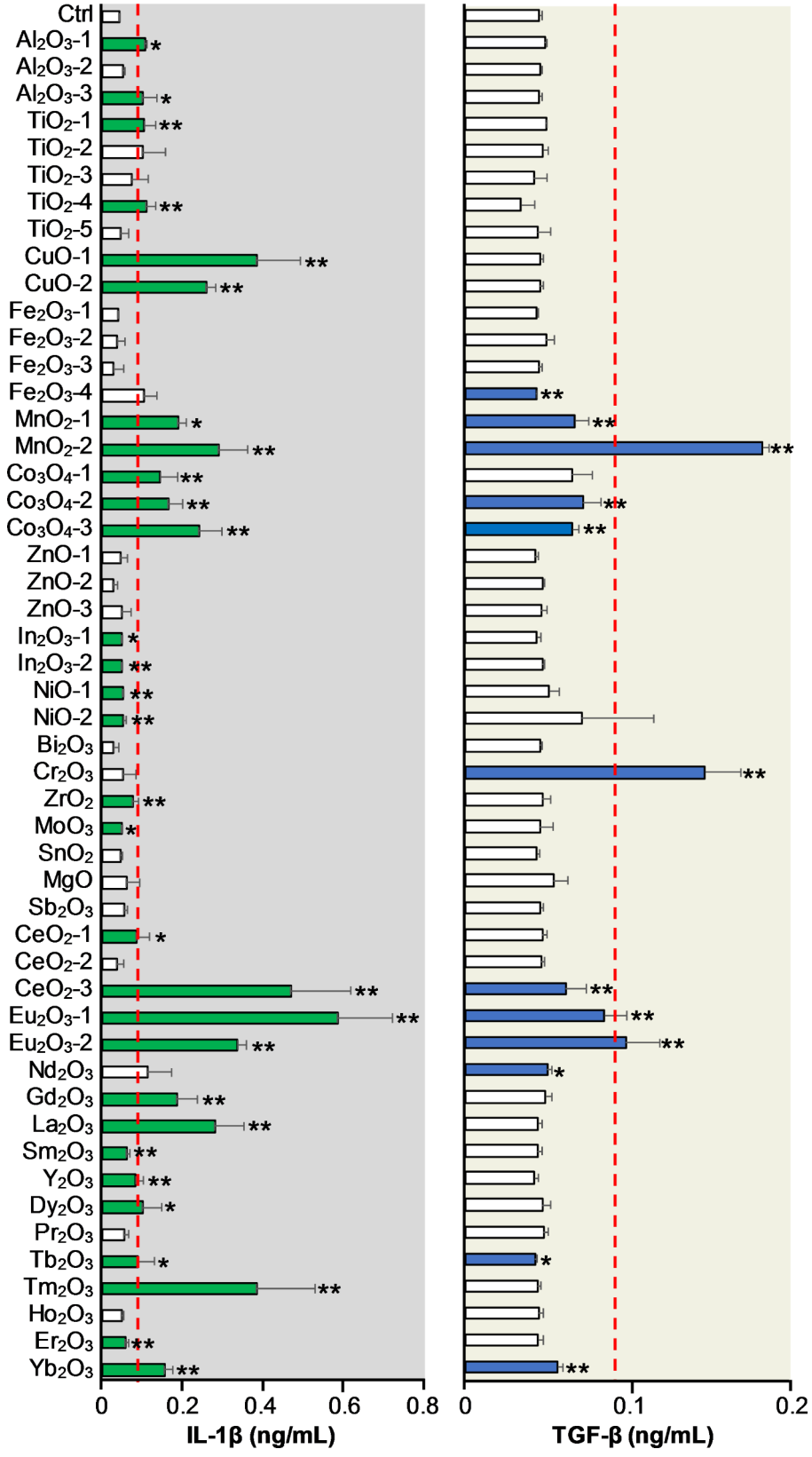

Fig. 4 The impacts of MeONPs on IL-1β and TGF-β1
THP-1 and BEAS-2B cells were exposed to 12.5 μg/mL MeONPs for 24 h. Then the IL-1β and TGF-β1 levels in the supernatants of THP-1 and BEAS-2B cells, respectively, were detected by ELISA ($n = 3$).*$p < 0.05$, **$p < 0.01$ compared to the control by two-tailed Student's T test

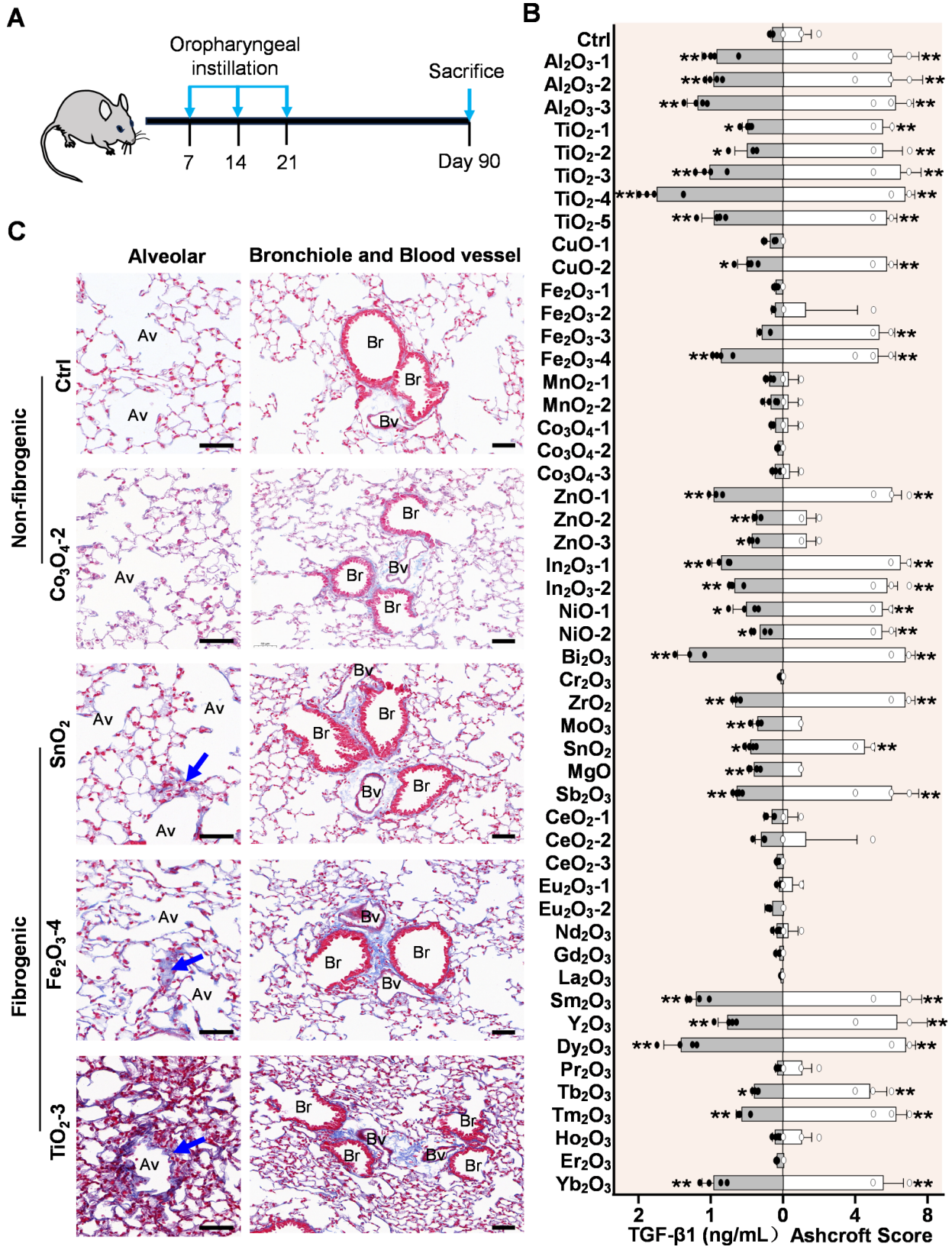

Fig. 5 (See legend on next page.)

(See figure on previous page.)

Fig. 5 Assessment of thefibrogenic potential of MeONPs in mouse lungs

(A) Schematic illustration of MeONP exposure in mice.Mice were exposed to 50 µL of PBS (vehicle ctrl) or MeONP suspension (2 mg/kg) by oropharyngeal aspiration every week for three times. The animals were sacrificed at the 90th day to collect BALF and lung tissues for further examinations. **(B)** TGF-β1 levels of MeONPs in BALF and Ashcroft scores of stained lung sections were determined to assess fibrogenic potential of MeONPs. **(C)** Representative images of Masson's trichrome staining of lung tissues exposed to MeONPs. BALFs were collected to measure TGF-β1 by ELISA ($n=3$ or 4). Lung tissues were collected and stained Masson's Trichrome staining according to a standard protocol. Ashcroft scores were used to estimate the collagen deposition levels in lung tissues ($n=3$ or 4). Blue arrows show the collagen deposition or pathologic change in Av. *$p<0.05$, **$p<0.01$ compared to the vehicle ctrl by two-tailed Student's t test. Scale bar represents 50 µm

Thirty MeONPs (Al_2O_3-1, Al_2O_3-3, TiO_2-1, TiO_2-2, TiO_2-4, CuO-1, etc.) induced significant IL-1β release even at a low dose of 12.5 µg/ml. Additionally, 10 MeONPs induced significant TGF-β1 production in BEAS-2B cells at dose of 12.5 µg/ml (Fig. 4), while the levels of other cytokines remained relatively low (Figure S3).

In vivo assessment of MeONP-induced fibrosis

To evaluate the in vivo fibrogenic potential of the 50 MeONPs, we administered them into the lungs of C57BL/6 mice once a week for three consecutive weeks at a dose of 2 mg/kg, and subsequently assessed lung fibrosis after three months (Fig. 5A). Recognizing the crucial role of TGF-β1 in promoting fibrosis, we determined the levels of active TGF-β1 in bronchoalveolar lavage fluid (BALF) using ELISA [36]. As depicted in Fig. 5B and Table S5, 29 MeONPs, including Al_2O_3-1, Al_2O_3-2, Al_2O_3-3, TiO_2-1, TiO_2-4, TiO_2-5, etc., induced a high level of TGF-β1 in BALF with fold change (FC) > 2. The other MeONPs showed very limited effects on the TGF-β1 release in mice lung. To examine the extent of pulmonary fibrosis, collagen deposition in tissues was visualized through trichrome staining of lung sections. As illustrated in Fig. 5C and Figure S4, lung sections from vehicle-treated animals exhibited minimal collagen deposits around small blood vessels (BV), bronchiole (Br) and alveolar (Av) areas. In contrast, exposure to fibrogenic MeONPs resulted in significant focal collagen deposits around some of these three architectures. The fibrogenic ranking of lung tissues was evaluated based on collagen staining images using the widely employed Ashcroft score [37]. Intriguingly, 25 MeONPs induced significant collagen deposition in mouse lungs with Ashcroft scores exceeding 2, consistent with the results of TGF-β1 levels (Fig. 5B). However, noteworthy inconsistencies were also observed. For instance, ZnO-3 induced significant TGF-β1 release but had negligible effects on collagen deposition, whereas Fe_2O_3-3 induced low TGF-β1 release but resulted in significant collagen deposition. Given these differences, both TGF-β1 and collogen deposition were considered in the assessment of MeONPs' fibrogenic potentials. A fibrogenic tag was assigned to a MeONP when $FC_{TGF-\beta1} \geq 2$ or Ashcroft score ≥ 2, while a non-fibrogenic tag was assigned otherwise. As a result, among all tested MeONPs, 30 were identified as fibrogenic, and 20 were classified as non-fibrogenic.

Identification of key descriptors for predicting lung fibrosis

Through a series of experimental analyses of MeONP interactions with simulated biofluids and cell models, we identified 18 quantitative in chemico and in vitro features, as detailed in Table 1. To unveil pivotal descriptors associated with MeONP-induced lung fibrosis, we employed a random forest (RF) classification analysis [36], integrating the acquired in chemico and in vitro features with in vivo fibrogenic indexes. Subsequently, seven features, namely IL-1β, NADH levels in THP-1 cells and epithelial cells, TGF-β1, dissolution in phagolysosomal simulated fluid (PSF), zeta potential, and hydrodynamic size of MeONPs, emerged as the top key features (Fig. 6). Notably, IL-1β was identified as the most important feature, contributing 27.8% to the model's prediction. Mitochondrial activity (specifically NADH levels) in macrophages followed closely with a contribution of 17.6%. The other five key features, include TGF-β1 release and NADH levels in epithelial cells, dissolution in lysosomal simulated fluids, zeta potential, and the hydrodynamic size of MeONPs, contributed 54.5% in total. A software named "Nano-induced Lung Fibrosis Prediction" (NILFP v 1.0.0) was developed based on the identified predictive descriptors, which is available at GitHub (https://github.com/huangyang2023/NILFPv1.0.0/releases/download/NILFPv1.0.0/NILFP.v1.0.0.zip) for fibrogenic risk assessment of untested MeONPs.

Discussion

The escalating volume of epidemiological studies underscores the potential of airborne fine particulates to instigate severe respiratory conditions, encompassing acute lung inflammation [38], fibrosis [39], and carcinogenesis [40, 41]. It is essential to acknowledge that NPs, with diverse physicochemical properties, can evoke various biological responses [9, 42, 43]. For example, Au NPs exhibit relative bio-inertness and safety [44], while ZnO NPs often induce cell death through ion release [45, 46]. Even NPs with identical chemical compositions may elicit distinct biological effects due to variations in properties like surface functionality, size, and crystallinity. For instance, graphene oxide (GO) nanosheets with elevated surface oxidation levels can lead to severe cell membrane damage, cell death, and acute lung inflammation, whereas reduced GOs demonstrate a comparatively safer profile [47].

Table 1 Nano-bio interactions related to lung fibrosis

Nano-bio interactions		Quantified feature
MeONP change	Aggregation	Hydrodynamic diameter
	Surface modification	Zeta potential
	Ion release	Dissolution in SLF
		Dissolution in PSF
Biological change	Membrane disruption	LDH release in macrophages*
		LDH release in epithelial cells*
	Lysosome dysfunction	Lysosomal pH in macrophages*
	Mitochondrial dysfunction	NADH level in macrophages*
		NADH level in epithelial cells*
		ATP level in macrophages*
		ATP level in epithelial cells*
	Redox homeostasis	ROS generation in macrophages*
		ROS generation in epithelial cells *
	Cytokine release	IL-1β release from macrophages*
		TNF-α release from macrophages*
		IL-6 release from macrophages*
		MCP-1 release from macrophages*
		TGF-β1 release from epithelial cells*

Note: *Features were quantified at five exposure doses: 12.5, 25, 50, 100 and 200 μg/ml

In this study, we specifically chose MeONPs, one of the most widely used types of NPs, to identify predictive descriptors for fibrosis, a manifestation of permanent and irreversible lung injury. Given the complex nano-bio interactions involved in MeONP-induced lung fibrosis, our objective was to thoroughly investigate the pulmonary trajectory of MeONPs through both radio-imaging of tissue distributions and confocal microscopy imaging of subcellular distributions, with La_2O_3 selected as a representative MeONP. The ^{125}I-labeled La_2O_3, CeO_2, Nd_2O_3 and ZnO were exclusively detected in mouse lungs. CeO_2, La_2O_3, and Nd_2O_3 shared a similar lung retention profile, persisting for up to 10 days, while ZnO showed a relatively rapid clearance within 5 days. Clearance of MeONPs from the lungs occurs slowly. While we observe a steady reduction in lung signal over time, the clearance pathways via the GI tract or bladder remain below the detection threshold of SPECT-CT, making it difficult to visualize particle transit through these organs. This sensitivity limitation likely accounts for the absence of visible signals indicating detailed particle clearance in other body parts. For an in-depth analysis of nano-bio interactions, TEM was employed to trace La_2O_3, revealing predominant localizations in alveoli or internalization by macrophages/epithelial cells near the air-blood barrier. Considering the air-blood barrier is covered by a thin layer of lung lining fluid comprising phospholipids and proteins, MeONPs are likely to interact with this fluid before establishing contact with epithelial cells. Confocal imaging illuminated the intracellular dynamics of MeONPs, encompassing interactions with the plasma membrane, lysosome, and other cytoplasmic constituents. This cellular fate aligns with observations in other nanoparticles, such as doped graphene nanosheets [48], up-conversion nanoparticles [49] and superparamagnetic iron oxide nanoparticles [50]. In combination, this tiered imaging approach enabled a comprehensive understanding of MeONP trajectories in animal lungs and the interpretation of diverse nano-bio interfaces.

In our exploration of MeONP interactions within mouse lungs, we aimed to understand nano-lung interactions by investigating the physicochemical changes of MeONPs in specific fluids and their impact on cellular functions. All examinations were conducted through either abiotic tests or cell experiments, avoiding animal use to facilitate high-throughput screenings. The observed aggregation and altered surface charges in SLF suggest potential changes in MeONP characteristics upon contact with pulmonary fluids. Elevated dissolution rates in PSF highlight the influence of acidic fluid on the chemical composition of MeONPs. These insights are crucial for comprehending the fate and transformations of MeONPs within the complex pulmonary microenvironment. Given that both macrophages and epithelial cells are primary targets for inhaled nanoparticles, we assessed the impacts of MeONPs on THP-1 and BEAS-2B cells. THP-1 cells provided insights into MeONPs' effects on pro-inflammatory cytokines, while BEAS-2B cells, an immortalized normal cell line, were used to gauge their impact on growth factor production. Our assessment of MeONP impacts on both cell lines revealed multifaceted effects, with variations in plasma membrane damage, lysosomal pH change, mitochondrial activity, ROS generation and cytokine release between THP-1 and BEAS-2B cells.

Interestingly, the in vivo administration of MeONPs yielded diverse fibrogenic outcomes. Considering its relevance to realistic exposure conditions and its effectiveness in distinguishing inter-material differences [51–53], a 2 mg/kg dose was administered via oropharyngeal aspiration. While some variability is inherent in this technique, particularly with less experienced operators, it allows for more precise dosing and requires less material compared to inhalation exposure, making it a practical and efficient choice for our study. The strong correlation (Pearson's coefficient factor at 0.84) between elevated TGF-β1 levels and collagen deposition underscores the potential role of TGF-β1 in MeONP-induced fibrosis. The designation of MeONPs as fibrogenic was based on either TGF-β1 upregulation (fold change ≥ 2) or histological evidence of collagen deposition (Ashcroft score ≥ 2), balancing early molecular signals with definitive tissue changes. While we acknowledge that TGF-β1 upregulation alone does not signify irreversible fibrosis, it reflects

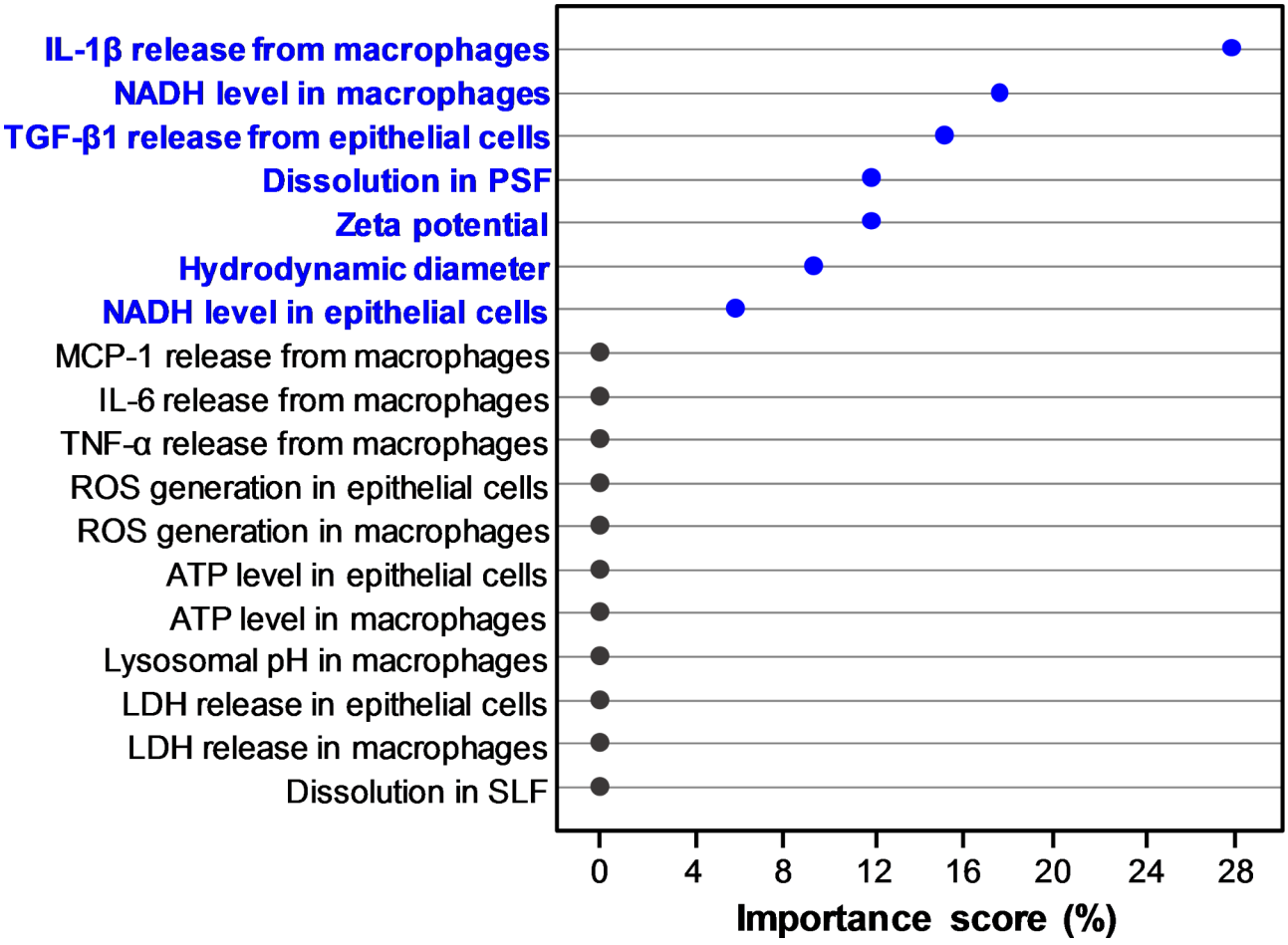

Fig. 6 Contributions of descriptors in predicting MeONP-induced lung fibrosis
RF classification analysis was performed to quantify the contributions of eighteen descriptors to MeONP-induced lung fibrosis. Seven descriptors, namely IL-1β release in macrophages, NADH levels in macrophages, TGF-β1 release in epithelial cells, dissolution in PSF, zeta potential, hydrodynamic size, and NADH levels in epithelial cells, were identified as pivotal features determining MeONP-induced lung fibrosis

activation of fibrotic signaling pathways that precede histological changes. By including both criteria, we aimed to capture MeONPs that exhibit either robust fibrogenic signaling or established histopathological markers within our study timeframe. However, notable exceptions among the tested MeONPs highlight the complexity of in vivo responses. For instance, ZnO-3 induced high TGF-β1 release without significant collagen deposition, while Fe_2O_3-3 induced low TGF-β1 release but significant collagen deposition. In addition, we observed that some MeONPs induced different levels of TGF-β1 in the BALF but exhibited same Ashcroft scores. For example, TiO_2-4 induced higher TGF-β1 levels than Al_2O_3 despite both MeONPs exhibiting the same Ashcroft scores. This discrepancy could be attributed to several factors: (i) the different dynamics of TGF-β1 production induced by Al_2O_3 and TiO_2-4, making it challenging to capture their peak values within the 90-day time frame; (ii) the differential impacts of Al_2O_3 and TiO_2-4 on growth factors (e.g., TGF, PDGF, EGF and FGF families) [54], with TGF-β1 potentially being less responsive to Al_2O_3 exposure.

Using TGF-β1 levels in BALF and Ashcroft scores of histology images, our analysis identified 30 fibrogenic MeONPs and 20 non-fibrogenic MeONPs. All tested MeONPs encompass 30 chemical compositions. Among them, the fibrogenic potentials of 8 MeONPs were consistent with literature reports, including 6 fibrogenic ones (TiO_2, ZnO, In_2O_3, NiO_2, Sb_2O_3 and Yb_2O_3) and 2 non-fibrogenic ones (MnO_2, and Co_3O_4) [22, 31, 55–60]. Significantly, our study reports, for the first time, the effects of 17 MeONPs on lung fibrosis, including Al_2O_3, Bi_2O_3, Cr_2O_3, ZrO_2, MoO_3, SnO_2, MgO, CuO, Eu_2O_3, Nd_2O_3, Sm_2O_3, Y_2O_3, Dy_2O_3, Pr_2O_3, Tb_2O_3, Tm_2O_3, and Ho_2O_3. Alongside chemical composition, hydrodynamic size, zeta potential, and dissolution rate emerged as top predictive descriptors of MeONP-induced lung fibrosis. This finding aligns with literature reports, where these physicochemical properties have been implicated in ENM-induced lung fibrosis [61–63]. For instance, previous

studies have highlighted the correlation between surface charge and fibrogenic potential, indicating higher fibrogenic effects with cationic nanotubes compared to anionic nanotubes [63]. Additionally, nanoparticle size has been linked to fibrosis severity, with larger nanoparticles often triggering more pronounced fibrotic responses due to their lower dissolution rates and prolonged biopersistence in the lungs [64].

The integration of in chemico and in vitro features with in vivo fibrogenic indexes through random forest classification unveiled crucial descriptors. IL-1β emerged as a key predictor, emphasizing its central role in MeONP-induced lung fibrosis. The combined importance of NADH levels, TGF-β1, dissolution rates, zeta potential, and hydrodynamic size further refines our understanding of the intricate relationship between MeONP characteristics and their fibrogenic potential. Accurate fibrogenic prediction requires a combination of these seven features rather than relying on one or two top indexes. For instance, while Eu_2O_3 and MnO_2 induced high levels of IL-1β and TGF-β1 in vitro, their contributions to mitochondrial activities (specifically NADH levels) in two cell lines, dissolution in lysosomal simulated fluids, zeta potential, or hydrodynamic size were comparatively lower, resulting in a lower fibrogenic potential in animals. The identified predictors of MeONP-induced lung fibrosis are closely aligned with two primary fibrogenic mechanisms: biopersistence and cellular damage. Biopersistence, reflecting the prolonged retention and stability of MeONPs within lung tissues, correlates with three in chemico predictors: zeta potential, hydrodynamic size, and dissolution in PSF. Specifically, MeONPs with positive surface charge, large size, and low dissolution rates tend to exhibit extended residence times in animal lungs, likely promoting sustained cellular interactions that contribute to chronic inflammation and fibrotic signaling. Parallelly, cellular damage is reflected by in vitro predictors such as IL-1β, TGF-β1, and NADH levels in THP-1 and BEAS-2B cells, which serve as indicators of cellular distress. Together, these predictors illustrate how both the physical persistence of MeONPs and their potential to induce direct cellular damage are crucial to their fibrogenic potential.

IL-1β, a pro-inflammatory cytokine, emerges as the most critical descriptor in predicting MeONP-induced lung fibrosis, aligning with previous studies indicating that certain fibrosis-inducing nanoparticles, such as SiO_2[65, 66] and rare earth oxide [67], tend to induce IL-1β in macrophages. While the precise mechanisms underlying the role of IL-1β in nanoparticle-induced lung fibrosis remain incompletely understood, IL-1β is recognized for its pivotal role in inflammation and tissue remodeling, fostering fibrosis development [68, 69]. This cytokine facilitates the recruitment and activation of immune cells, including neutrophils and monocytes [70], with inflammation often initiating pulmonary pathogenic changes in lung fibrosis. Furthermore, IL-1β stimulates the production of other pro-inflammatory cytokines, chemokines, and fibrotic factors, contributing to lung fibrosis [71]. Additionally, IL-1β promotes the production of TGF-β1, a key direct regulatory factor in lung fibrosis development [68]. Specifically, TGF-β induces fibroblast differentiation into myofibroblasts, highly contractile cells implicated in tissue remodeling and fibrosis [72]. Notably, TGF-β1 is also identified as a contributor in our prediction model. Alongside cytokines, the dose-dependent decrease in NADH levels in both macrophages and epithelial cells emerges as a significant contributor to MeONP-induced lung fibrosis, suggesting the occurrence of disrupted cellular metabolism in the processes of lung fibrosis.

The physicochemical properties of MeONPs, including size, zeta potential, and dissolution, contribute 33.4% to the overall feature importance. We propose that these three descriptors are closely linked to the bio-persistence of MeONPs. The adverse outcomes of MeONPs are often influenced by their biological distribution and fate. While most intratracheally instilled (IT) MeONPs have prolonged retention in the lungs, they can also spread to other tissues and organs. Konduru et al. demonstrated this with isotopically labeled IT ZnO, finding ZnONPs in skeletal muscle, liver, skin, kidneys, cecum, blood, and bone [73]. This systemic distribution of ZnO could be attributed to either the release of Zn ions from ZnONPs or the crossing of ZnONPs through the air-blood barrier. The localized retention of NPs in the lungs can lead to interactions with pulmonary cells, particularly epithelial cells and macrophages, potentially triggering acute lung inflammation [33] or chronic lung injuries such as fibrosis [63, 67] and carcinogenesis [15]. In contrast, systemically distributed MeONPs may lead to toxicities in remote organs or tissues, such as cardiovascular disease [12], reproductive disorders [13], and neurological disorders [14].

The inhaled MeONPs initially interact with the mucus layer in the conducting airway, composed of water, mucins, lipids, salts, and cellular debris. In the conducting airway, large MeONP agglomerates could be efficiently cleared. However, small particles, particularly cationic ones, can penetrate the gas-exchange airways, notably the alveoli, interacting with a thin layer of pulmonary surfactant-a complex mixture primarily composed of lipids (such as phospholipids and cholesterol) and proteins (surfactant proteins A, B, C, and D). The interaction of MeONPs with the mucus layer and pulmonary surfactant can alter their surface charge, aggregation, and corona formation, influencing their biological fate. For instance, Konduru et al. found that the corona

constituents of $BaSO_4$, ZnO and CeO_2 have significant differences [74]. The amounts of albumin, transferrin and α-1 antitrypsin in the coronas of $BaSO_4$ and ZnO are higher than that of CeO_2 NPs, which may affect their uptake by macrophages. While assessing the effects of relevant fluids on the biological behavior of MeONPs could better align with their travel path, this may require the sacrifice of animals to collect BALF, which is conflict with the principles of the 3Rs (Replacement, Reduction, Refinement) in animal testing as well as the primary goal of our study: using animal-free tests to predict the fibrogenic potential of MeONPs.

Small particles penetrated the deep lung alveoli can also interact with lung cells. Within cell lysosomes, particle dissolution emerges as a critical factor influencing their clearance. Nanoparticles with high dissolution capabilities, like ZnO, could be rapidly cleared from the lungs. Therefore, most small-sized, cationic, and insoluble MeONPs are presumed to exhibit prolonged biopersistence, illustrated by Al_2O_3, In_2O_3, and ZrO_2. This aligns with studies demonstrating that ultrafine particles induce more significant pulmonary inflammation in rat models compared to fine particles of the same composition on an equal mass-dose basis [75]. Moreover, cationic carbon nanotubes were reported to induce higher fibrosis than tubes with anionic and neutral surface charges [63]. However, these general principles cannot be universally applied to all MeONPs. For instance, ZnO-1, despite its high dissolution capability, induced significant collagen deposition due to its pronounced cytotoxicity. Conversely, CeO_2-1 and CeO_2-1, characterized by low dissolution, cationic charge, and small size, exhibited low fibrogenic potential as it had limited effects on IL-1β and NADH. Beyond the physicochemical properties of MeONPs, our study emphasizes the critical role of a descriptor formula in nanoparticle-induced pulmonary fibrosis. NILFP was developed based on the identified descriptor formula for fibrogenic risk assessment of MeONPs, MeONP-based nanoproducts and beyond.

Conclusion

The study successfully identified key in chemico and in vitro descriptors in MeONP-induced lung fibrosis in animals, providing valuable insights into the intricate behavior of MeONPs. By employing radiological and fluorescent labeling on a representative MeONP, La_2O_3, we uncovered its prolonged retention in mouse lungs and delineated its intracellular trajectory. The interactions of 50 MeONPs with simulated biofluids exhibited diverse behaviors in hydrodynamic size, Zeta potential, and dissolution rate. MeONPs induced variable effects on cellular functions, affecting plasma membrane integrity, lysosomal pH, mitochondrial activity, oxidative stress, and cytokine production, with distinct responses observed in different cell lines. In vivo assessments of fibrogenic potential revealed diverse outcomes, with 29 MeONPs inducing high TGF-β1 levels and 25 of which causing significant collagen deposition in lung tissues. The application of random forest classification analysis to in chemico, in vitro and in vivo data enabled the identification of seven crucial predictive descriptors determining MeONP interactions and outcomes. These descriptors include IL-1β, mitochondrial activities in two cell types, TGF-β1, dissolution in lysosomal simulated fluids, zeta potential, and hydrodynamic size of MeONPs. Notably, IL-1β emerged as the most critical descriptor, contributing 27.8% to the overall feature importance, followed by macrophage mitochondrial activity at 17.6%. The identification of these predictive descriptors derived from animal-free tests holds great promise for advancing the development of in silico models for nanoparticle-induced lung fibrosis.

Materials and methods

Reagents and materials

MTS and ATP colorimetric assay kits were purchased from Promega (Madison, WI, USA). Gibco fetal bovine serum (FBS), Hoechst 33,342, dichlorodihydrofluorescein diacetate (DCFH-DA), LysoTracker Red DND-99 and WGA-594 were obtained from Thermo Fisher Scientific (Grand Island, NY, USA). IL-1β, IL-6, TNF-α, and MCP-1 ELISA Kits were from BD biosciences (San Jose, CA, USA). TGF-β1 ELISA Kit was from R&D Systems (Minneapolis, MN, USA). RPMI 1640 medium was purchased from Corning Inc. (New York, NY, USA). Bronchial epithelial cell medium (BepiCM) was from Sciencell (San Diego, CA, USA). Penicillin, streptomycin, and trypsin-EDTA were purchased from HyClone Laboratory (South Logan, UT, USA). ^{125}I was from GMS Pharmaceutical Corporation (Shanghai, China). All the MeONPs (not coated) were in-house synthesized or obtained from Aladdin Scientific Corporation (Shanghai, China), as detailed in Table S1.

Material characterization

The morphologies and primary sizes of MeONPs were measured by a transmission electron microscopy (TEM, Tecnai G2 spirit BioTwin, FEI, USA) at a voltage of 120 kV. TEM samples were prepared by placing a drop of MeONP suspensions (50 μg/mL in DI H_2O) on 200-mesh copper grids with carbon-coated formvar support films (Ted Pella, Inc.), which was left to air dry at room temperature.

Radiological or fluorescent labeling of MeONPs

Radiological ^{125}I labeled nanoparticles were prepared by a standard activator oxidation method in a radioactivity laboratory of the State Key Laboratory of Radiation

Medicine and Protection, Suzhou, China. Briefly, 1,3,4,6-tetrachloro-3 A,6 A- diphenylglycouril in trichloromethane (0.5 mg/mL) was dried under N2 blowing, and then incubation with 500 μL nanoparticle suspensions (1.65 mg/mL in DI H_2O) and 1 mCi of $Na^{125}I$ at 37 °C for 30 min. ^{125}I labeled nanoparticles were obtained by ultrafiltration with a 10 kDa membrane at 3000 rpm for 30 min and then re-suspended in 500 μL DI H_2O for radiological imaging.

FITC labeled nanoparticles were synthesized by an amidation reaction. In brief, EDC (10 mg) and NHS (20 mg) were added into 4 mL of nanoparticle suspensions (100 μg/mL) in DI H_2O and stirred for 2 h at 25 °C. After centrifugation at 20,000 rpm for 10 min, the particle pellets were collected to react with 1 mL of FITC solution (0.1 mg/mL) under magnetic stirring for 2 h. Finally, FITC labeled nanoparticles were collected by centrifugation and washed by DI H_2O for three times to remove non-covalent bound FITC. The resulted nanoparticles were re-suspended in 400 μL DI H_2O for further use.

SPECT/CT imaging of mice

Eight-week-old female C57BL/6 mice were purchased from Nanjing Peng Sheng Biological Technology (Nanjing, China). Animals were housed under standard laboratory conditions (25 °C; 60% relative humidity; 12 h light, 12 h dark cycle) and hygiene status (autoclaved food and acidified water) according to Soochow University guidelines for the care and treatment of laboratory animals. Animals were anesthetized by intraperitoneal injection of sodium pentobarbital (200 mg/kg) and exposed to ^{125}I labeled nanoparticles (300 μCi) by an oropharyngeal aspiration method. SPECT/CT imaging of the animals were performed on day 0, day 1, day 5, day 10, day 14 and day 18 by a U-SPECT+system (MILabs, Utrecht, the Netherlands) with an extra ultra-high sensitivity collimator (54 pinholes, reconstructed resolution 1.0 mm, sensitivity ≫12,500 cps/MBq).

TEM imaging of lung tissues

Female C57BL/6 mice were exposed to La_2O_3 nanoparticles at a dose of 2 mg/kg by oropharyngeal aspiration. After 24 h of exposure, the mice sacrificed by overdose of sodium pentobarbital (400 mg/kg). A piece of lung tissue was cut from the middle lobe of lungs and fixed in 2% glutaraldehyde in PBS for 4 h, following by postfixation in 1% osmium tetroxide in PBS for 1 h. Tissues were dehydrated through graded series of ethanol and propylene oxide, and then embedded in Epon. Lung sections were cut with an ultramicrotome and placed onto copper grids. The sections were stained with uranyl acetate and lead nitrate before examining on a JEOL transmission electron microscope at 80 kV, as previously reported.

Confocal imaging

THP-1 cells were primed by phorbol 12-myristate 13-acetate (PMA, 1 μg/mL) for 16 h and incubated with FITC-labeled La_2O_3 nanoparticles (50 μg/mL) for 0, 4, 6, 12 and 24 h. Then cells were collected and washed with phosphate-buffered saline for three times. To visualize the nuclei, membrane and lysosomes, the cells were fixed and stained with Hoechst 33,342 (100 ng/mL), WGA-594 and LysoTracker DND-99. All the cell samples were observed by a UltraViewVoX confocal microscope (PerkinElmer, USA).

Characterization of the biotransformation of MeONPs in biological fluid

The hydrodynamic diameters and surface charges of MeONP dispersions were determined by dynamic light scattering and zeta potential analysis on a Zetasizer Nano ZS90 (Malvern Instruments Corp., UK) instrument. To assess the dissolution capabilities of MeONPs in phagolysosomal simulated fluid (PSF) and simulated lung fluid (SLF), MeONPs were dissolved in 10 mL PSF or SLF buffer at concentration of 50 μg/mL, followed by probe sonication at 32 W for 10 s. PSF was prepared by dissolving 142 mg/L Na_2HPO4, 6.65 g/L NaCl, 62 mg/L Na_2SO_4, 29 mg/L $CaCl_2{\cdot}H_2O$, 250 mg/L glycine, 8.09 g/L potassium phthalate in DI H_2O (pH 4.5). SLF was a solution of 95 mg/L $MgCl_2$, 6.019 g/L NaCl, 298 mg/L KCl, 126 mg/L Na_2HPO_4, 63 mg/L Na_2SO_4, 368 mg/L $CaCl_2{\cdot}2H_2O$, 574 mg/L CH_3COONa and 2.604 g/L $NaHCO_3$, 97 mg/L sodium citrate dihydrate (pH 7.4). The stability of all MeONP suspensions was assessed by measuring their specific absorbance values across the 300–700 nm range. All suspensions reached a stable phase after 12 h. Following a 24-hour incubation at 25 °C, the supernatants of the MeONP suspensions were collected by centrifugation at 15,000 rpm for 10 min. For comparison, vehicle blanks containing only PSF or SLF were included and subjected to the same treatments. The concentrations of metal ions in supernatants were measured using an inductively coupled plasma-atomic emission spectrometry (ICP-OES, ICPE-9000, Shimadzu Corp.). The percentages of MeONP dissolution were calculated using the following equation:

$$\text{Dissolution} = \frac{C}{50 * R} \times 100\%$$

where C (μg/mL) is the concentration of metal ions in supernatants; R is the mass ratio of metal elements in each MeONPs.

Assessment of impacts of MeONP on cells

To minimize variability across experimental batches and to focus on the relative cellular responses induced by each MeONP, all 50 MeONPs were tested simultaneously using the same batch of cell samples. THP-1

and BEAS-2B cells were seeded at a density of 3×10^4 cells/well and 8×10^3 cells/well, respectively, in 96-well plates. THP-1 cells were cultured in RPMI 1640 medium supplemented with 10% fetal bovine serum (Gemini, Woodland, USA), while BEAS-2B cells were cultured in BEpicM (Sciencell, San Diego, USA). After overnight incubation, the cell culture media in the 96-well plates were replaced with 100 μL aliquots of MeONP suspensions at concentrations of 0, 12.5, 25, 50, 100, and 200 μg/mL. A single control was consistently used for each plate across all experiments for the 50 MeONPs. Following a 24-hour incubation at 37 °C, the cells and supernatants were collected to evaluate the effects of MeONP on cellular contents. For THP-1 cells, the supernatants were collected to detect the release of lactate dehydrogenase (LDH) and cytokines, including TNF-α, IL-1β, IL-6, and MCP-1. The supernatants of BEAS-2B cells were used to measure LDH and TGF-β1 release. The limit of detection (LOD) for cytokine measurements is as follows: 3.9 pg/mL for IL-1β, 7.8 pg/mL for TNF-α, 4.7 pg/mL for IL-6, 31.2 pg/mL for TGF-β1, and 15.6 pg/mL for MCP-1. The MTS assay for detection of NADH in cells was performed by incubating the remaining cells with 120 μL of MTS working solution (5 mg/mL) in phenol red-free media for 2 h at 37 °C. The absorbance at 490 nm was then recorded using a microplate reader (BioTek, Synergy neo, USA). For the DCF assay, the cells were incubated with 15 μg/mL H_2DCF-DA in the dark for 30 min at 37 °C. The fluorescence of DCF was examined using an excitation wavelength of 488 nm on a microplate reader. After removing the DCF solution, the remaining cells were collected and lysed for ATP assay. For detection of lysosomal pH, cells were incubated with 100 μL Lysosensor Yellow/Blue DND-160 at 37 °C for 3 min. After washing by PBS for twice, the fluorescence of DND-160 was examined using an excitation wavelength of 540 nm on a microplate reader.

Assessment of lung fibrosis in mice

A total of 200 animals (C57Bl/6 female mice at 8 weeks) were used to determine chronic lung fibrosis induced by 50 different MeONPs, with four in parallel in each group. Additionally, we included 8 control mice, divided into two separate control groups: 4 mice received PBS, and 4 mice were administered quartz as a positive control for fibrosis induction. Animals were housed under standard laboratory conditions. The treatment protocols were approved as following Soochow University Laboratory Animal Center protocols. All animal experiments were approved by the Ethics Committee of Soochow University (202108A0134). Animals were exposed to MeONPs by an oropharyngeal aspiration method. Briefly, MeONPs were suspended in PBS at 1 mg/mL by a probe sonication (32 W) for 10 s in an ice-water bath. The stability of the MeONP suspensions was assessed by measuring absorbance changes across 300–700 nm. Probe sonication maintained suspension stability with less than a 2% decline over 10 min, allowing each MeONP suspension to be promptly instilled into the animal lungs within 10 min post-sonication. The animals were anesthetized by intraperitoneal injection of sodium pentobarbital (200 mg/kg) in a total volume of 100 uL. The anesthetized animals were held in a vertical position, with their noses blocked to enforce breathing through the mouth. The MeONP suspensions (administered at a dose of 2 mg/kg) were applied to the back of the tongue using a standard oropharyngeal aspiration technique [76]. Animals in the vehicle and positive control groups received 50 uL of PBS and 2 mg/kg quartz, respectively. To estimate the aspiration dose of MeONPs in mice, we employed two formulas based on occupational exposure scenarios [52, 77, 78]:

$$SMD = \frac{OEC \times MV \times T \times DF}{SA} \quad (1)$$

$$AD = \frac{SMD \times SA}{W} \quad (2)$$

Where, SMD: Surface mass density (mg/m^2). OEC: Occupational Exposure Concentration (mg/m^3), assumed as 5 mg/m^3 based on the threshold limit for welding fumes by NIOSH [79]. MV: minute ventilation, assumed as 0.02 m^3/min for a human adult [77, 78]. T: Duration of exposure (480 min/day). DF: deposition fraction, assumed as 30% for nanoparticles. SA: lung surface area, assumed as 102 m^2 for humans and 0.05 m^2 for mice [77]. W: mouse body weight, assumed as 0.025 kg. Using these parameters, human exposure over a month (20 working days) would yield an SMD of 2.82 mg/m^2 and an AD of 5.64 mg/kg. In our study, the animals were exposed to a total of 6 mg/kg MeONPs (2 mg/kg per dose administered three times). This dose is comparable to the calculated human-equivalent dose and aligns with occupational exposure levels under high-end scenarios, such as in industries with poorly controlled nanoparticle emissions.

Mice underwent exposures once a week over three weeks and were euthanized on day 90 with a sodium pentobarbital overdose (400 mg/kg). Bronchoalveolar lavage fluids (BALFs) and lung tissues were collected following established protocols [42], the trachea was cannulated, and the lungs were gently lavaged three times with 1 mL of sterile PBS to collect BALF. A 50 μL aliquot of each BALF sample was used to determine TGF-β1 concentrations via ELISA kits (BDLISA, China). Lung tissues were collected and stained Masson's Trichrome staining according to a standard protocol. Ashcroft scores were used to estimate the collagen deposition levels

according to the method reported by Ashcroft et al. [37]. In detail, the whole lung sections were examined under a microscope at 10x magnification. Each field of view was assessed for interstitial fibrosis severity, scored from 0 to 8 using a predetermined scale. The predominant level of fibrosis occupying more than half of the field area was recorded. Normal tissue received a score of 0, while fibrotic tissue was categorized into odd-numbered severity levels. The criteria for scoring fibrosis were: 0-normal lung; 1-minimal thickening of walls of alveolar or bronchiole; 2 and 3-moderate thickening without damage; 4 and 5-increased fibrosis with structural damage; 6 and 7-severe distortion or large fibrous areas; 8-total fibrous obliteration. The mean score of all fields examined was taken as the Ashcroft score for the section.

Statistical analysis

All of the results were shown by mean±SD. Statistical significance between each MeONP treatment group and the control group was evaluated using two-tailed Student's T test. Unless otherwise noted, at least three independent experiments were performed for abiotic and cell experiments, and statistical significances were set at $p<0.05$. Random forest (RF) classification analysis was performed on Weka software (Ver 3.8.5). The 30 fibrogenic MeONPs and 20 non-fibrogenic MeONPs were randomly split into training and test set, with 40 in the training set and the rest in test set. For each MeONP, all its in vitro and in vivo data points were included in either the training set or the test set. Classification model was built using the training set. To assess the prediction accuracy of the models and avoid overfitting, 10-fold cross-validation was performed in the training set. External validation was performed in the test set.

Supplementary Information

The online version contains supplementary material available at https://doi.org/10.1186/s12989-024-00616-3.

Supplementary Material 1

Acknowledgements

Not applicable.

Author contributions

J.C., Y.Y., X.C. and R.L. conceived and designed the study. J.C. and Y.Y. performed most of the experiments and participated in the writing of manuscript. Y.H., X.L. and N.A. performed Random Forest classification and data analysis. X.L. and M.N. performed the nanoparticle characterization. D.W. participated in ELISA tests. Q.X. and A.K. participated in the studies about assessment of lung fibrosis in mice. The writing of the paper was led by X.C. and R.L. with participation from J.C. and Y.Y.

Funding

This work was supported by the grants from the National Key R&D Program of China (2022YFE0124000), the financial support of the European Union under the Refresh-Research Excellence for Region Sustainability and High-tech Industries project (CZ.10.03.01/00/22_003/0000048) via the Operational Programme Just Transition.

Data availability

The data that support the findings of this study are available from the corresponding author upon reasonable request.

Declarations

Ethics approval

All animal experiments were approved by the Ethics Committee of Soochow University (202108A0134).

Competing interests

The authors declare no competing interests.

Author details

[1]School of Public Health, Suzhou Medical School, Soochow University, Suzhou, Jiangsu 215123, China
[2]State Key Laboratory of Radiation Medicine and Protection, School of Radiation Medicine and Protection, Suzhou Medical School, Soochow University, Suzhou, Jiangsu 215123, China
[3]Key Laboratory of Industrial Ecology and Environmental Engineering (MOE), Dalian Key Laboratory on Chemicals Risk Control and Pollution Prevention Technology, School of Environmental Science and Technology, Dalian University of Technology, Dalian 116024, China
[4]Department of Biological Chemistry, Belarusian State Medical University, Minsk 220089, Belarus
[5]B.I. Stepanov Institute of Physics of National Academy of Sciences of Belarus, 68Nezalezhnasti Ave, Minsk 220072, Belarus
[6]Department of Chemistry, University of Malta, Msida 2080, MSD, Malta
[7]CEET, Nanotechnology Centre, VSB-Technical University of Ostrava, 17 listopadu, Ostrava 2172-15, 70800, Czech Republic

Received: 16 August 2024 / Accepted: 11 December 2024
Published online: 14 January 2025

References

1. Fytianos G, Rahdar A, Kyzas GZ. Nanomaterials Cosmetics: Recent Updates Nanomaterials. 2020;10(5):16.
2. Carley LN, Panchagavi R, Song X, Davenport S, Bergemann CM, McCumber AW, Gunsch CK, Simonin M. Long-Term Effects of Copper Nanopesticides on Soil and Sediment Community Diversity in Two Outdoor Mesocosm Experiments. Environ Sci Technol. 2020;54(14):8878–89.
3. Couto C, Almeida A. Metallic Nanoparticles in the Food Sector: A Mini-Review. Foods. 2022;11(3):22.
4. Joseph TM, Mahapatra DK, Esmaeili A, Piszczyk L, Hasanin MS, Kattali M, Haponiuk J, Thomas S. Nanoparticles: Taking a Unique Position in Medicine. Nanomaterials 2023, 13 (3), 58.
5. Pomerantseva E, Bonaccorso F, Feng XL, Cui Y, Gogotsi Y. Energy storage: The future enabled by nanomaterials. Science. 2019;366(6468):eaan8285.
6. Yao J, Zou FL, Feng J, You RT, Sun JX, Zhang XF, Xiang Y. Z., 3D printing technology based on nanometer materials in mechanical automation processing. Ferroelectrics. 2021;578(1):81–94.
7. Haruna S, Adamu M, Ibrahim YE, Haruna SI, ElDin HMS, Hamza MF, Azab M. Multifunctional engineered cementitious composites modified with nanomaterials and their applications: An overview. Rev Adv Mater Sci. 2023;62(1):15.
8. Nanotechnology Products Database. https://product.statnano.com/. (accessed 10/10/2023).
9. Semenzin E, Subramanian V, Pizzol L, Zabeo A, Fransman W, Oksel C, Hristozov D, Marcomini A. Controlling the risks of nano-enabled products through the life cycle: The case of nano copper oxide paint for wood protection and nano-pigments used in the automotive industry. Environ Int. 2019;31:104901.
10. Xia T, Zhu YF, Mu LN, Zhang ZF, Liu SJ. Pulmonary diseases induced by ambient ultrafine and engineered nanoparticles in twenty-first century. Natl Sci Rev. 2016;3(4):416–29.
11. Wu WD, Jin YF, Carlsten C. Inflammatory health effects of indoor and outdoor particulate matter. J Allergy Clin Immunol. 2018;141(3):833–44.

12. Brook DR, Rajagopalan S, Pope CA 3rd, Brook RJ, Bhatnagar A, Diez-Roux VA, Holguin F, Hong YL, Luepker VR, Murray A, Mittleman AM, Peters A, Siscovick D, Smith CS Jr, Whitsel L, Kaufman DJ. Particulate matter air pollution and cardiovascular disease: An update to the scientific statement from the American Heart Association. Circulation. 2010;121(21):2331–78.
13. Wang RL, Song B, Wu JR, Zhang YL, Chen AJ, Shao LQ. Potential adverse effects of nanoparticles on the reproductive system. Int J Nanomed. 2018;11(13):8487–506.
14. O'Piela DR, Durisek GR 3rd, Escobar ., Mackos YH, Wold AR. Particulate matter and Alzheimer's disease: an intimate connection. Trends Mol Med. 2022;28(9):770–80.
15. Hill W, Lim EL, Weeden CE, Lee C, Augustine M, Chen K, Kuan FC, Marongiu F, Evans EJ, Moore DA, Rodrigues FS, Pich O, Bakker B, Cha HG, Myers R, van Maldegem F, Boumelha J, Veeriah S, Rowan A, Naceur-Lombardelli C, Karasaki T, Sivakumar M, De S, Caswell DR, Nagano A, Black JRM, Martínez-Ruiz C, Ryu MH, Huff RD, Li S, Favé MJ, Magness A, Suárez-Bonnet A, Priestnall SL, Lüchtenborg M, Lavelle K, Pethick J, Hardy S, McRonald FE, Lin MH, Troccoli CI, Ghosh M, Miller YE, Merrick DT, Keith RL, Al Bakir M, Bailey C, Hill MS, Saal LH, Chen Y, George AM, Abbosh C, Kanu N, Lee SH, McGranahan N, Berg CD, Sasieni P, Houlston R, Turnbull C, Lam S, Awadalla P, Grönroos E, Downward J, Jacks T, Carlsten C, Malanchi I, Hackshaw A, Litchfield K, Lester. Nature. 2023;616(7955):159–67., J. F.; DeGregori, J.; Jamal-Hanjani, M.; Swanton, C., Lung adenocarcinoma promotion by air pollutants.
16. Jederlinic PJ, Abraham JL, Churg A, Himmelstein JS, Epler GR, Gaensler EA. Pulmonary fibrosis in aluminum oxide workers. Investigation of nine workers, with pathologic examination and microanalysis in three of them. Am Rev Respir Dis. 1990;142(5):1179–84.
17. Taiwo OA, Sircar KD, Slade MD, Cantley LF, Vegso SJ, Rabinowitz PM, Fiellin MG, Cullen M. R.,Incidence of asthma among aluminum workers. J Occup Environ Med. 2006;48(3):275–82.
18. Kraus T, Schaller KH, Angerer J, Hilgers RD, Letzel S. Aluminosis–detection of an almost forgotten disease with HRCT. J Occup Med Toxicol. 2006;1:4.
19. Björ O, Damber L, Edström C, Nilsson T. Long-term follow-up study of mortality and the incidence of cancer in a cohort of workers at a primary aluminum smelter in Sweden. Scand J Work Environ Health. 2008;34(6):463–70.
20. Schulte PA, Veruscka Leso V, Niang M, Iavicoli I. Current state of knowledge on the health effects of engineered nanomaterials in workers: a systematic review of human studies and epidemiological investigations. Scand J Work Environ Health. 2019;45(3):217–38.
21. Cho WS, Duffin R, Howie SEM, Scotton CJ, Wallace WAH, MacNee W, Bradley M, Megson IL, Donaldson K. Progressive severe lung injury by zinc oxide nanoparticles; the role of Zn^{2+} dissolution inside lysosomes. Part Fibre Toxicol. 2011;8:16.
22. Wu WT, Ichihara G, Hashimoto N, Hasegawa Y, Hayashi Y, Tada-Oikawa S, Suzuki Y, Chang J, Kato M, D'Alessandro-Gabazza CN, Gabazza EC, Ichihara S. Synergistic Effect of Bolus Exposure to Zinc Oxide Nanoparticles on Bleomycin-Induced Secretion of Pro-Fibrotic Cytokines without Lasting Fibrotic Changes in Murine Lungs. Int J Mol Sci. 2015;16(1):660–76.
23. Ma JY, Mercer RR, Barger M, Schwegler-Berry D, Scabilloni J, Ma JK, Castranova V. Induction of pulmonary fibrosis by cerium oxide nanoparticles. Toxicol Appl Pharmacol. 2012;262(3):255–64.
24. Schwotzer D, Ernst H, Schaudien D, Kock H, Pohlmann G, Dasenbrock C, Creutzenberg O. Effects from a 90-day inhalation toxicity study with cerium oxide and barium sulfate nanoparticles in rats. Part Fibre Toxicol. 2017;14:20.
25. Horváth T, Papp A, Kiricsi N, Igaz N, Trenka V, Kozma G, Tiszlavicz L, Rázga Z, Vezér T. Investigation of the effect of titanium dioxide nanorods on the lungs in a subacute rat model. Orv Hetil. 2019;160(2):57–66.
26. Hansen SF, Lennquist A. Carbon nanotubes added to the SIN List as a nanomaterial of Very High Concern. Nat Nanotechnol. 2020;15(1):3–4.
27. Heller DA, Jena PV, Pasquali M, Kostarelos K, Delogu LG, Meidl RE, Rotkin SV, Scheinberg DA, Schwartz RE, Terrones M, Wang YH, Bianco A, Boghossian AA, Cambré S, Cognet L, Corrie SR, Demokritou P, Giordani S, Hertel T, Ignatova T, Islam MF, Iverson NM, Jagota A, Janas D, Kono J, Kruss S, Landry MP, Li Y, Martel R, Maruyama S, Naumov AV, Prato M, Quinn SJ, Roxbury D, Strano MS, Tour JM, Weisman RB, Wenseleers W, Yudasaka M. Banning carbon nanotubes would be scientifically unjustified and damaging to innovation. Nat Nanotechnol. 2020;15:164–6.
28. Fadeel B, Farcal L, Hardy B, Vázquez-Campos S, Hristozov D, Marcomini A, Lynch I, Valsami-Jones E, Alenius H, Savolainen K. Nat Nanotechnol. 2018;13(7):537–43. Advanced tools for the safety assessment of nanomaterials.
29. Wyrzykowska E, Mikolajczyk A, Lynch I, Jeliazkova N, Kochev N, Sarimveis H, Doganis P, Karatzas P, Afantitis A, Melagraki G, Serra A, Greco D, Subbotina J, Lobaskin V, Bañares MA, Valsami-Jones E, Jagiello K, Puzyn T. Representing and describing nanomaterials in predictive nanoinformatics. Nat Nanotechnol. 2022;17(9):924–32.
30. Oh E, Liu R, Nel A, Gemill KB, Bilal M, Cohen Y, Medintz IL. Meta-analysis of cellular toxicity for cadmium-containing quantum dots. Nat Nanotechnol. 2016;11(5):479–86.
31. Li RB, Ji ZX, Qin HQ, Kang XD, Sun BB, Wang MY, Chang CH, Wang X, Zhang HY, Zou HF, Nel AE, Xia T. Interference in Autophagosome Fusion by Rare Earth Nanoparticles Disrupts Autophagic Flux and Regulation of an Interleukin-1β Producing Inflammasome. ACS Nano. 2014;8(10):10280–92.
32. Yazdi AS, Guarda G, Riteau N, Drexler SK, Tardivel A, Couillin I, Tschopp J. Nanoparticles activate the NLR pyrin domain containing 3 (Nlrp3) inflammasome and cause pulmonary inflammation through release of IL-1α and IL-1β. Proc Natl Acad Sci U S A. 2010;107(45):19449–54.
33. Huang Y, Li XH, Xu SJ, Zheng HZ, Zhang LL, Chen JW, Hong HX, Kusko R, Li RB. Quantitative Structure-Activity Relationship Models for Predicting Inflammatory Potential of Metal Oxide Nanoparticles. Environ Health Perspect. 2020;128(6):13.
34. Ryman-Rasmussen JP, Cesta MF, Brody AR, Shipley-Phillips JK, Everitt JI, Tewksbury EW, Moss OR, Wong BA, Dodd DE, Andersen ME, Bonner JC. Inhaled carbon nanotubes reach the subpleural tissue in mice. Nat Nanotechnol. 2009;4(11):747–51.
35. Hinderliter PM, Minard KR, Orr G, Chrisler WB, Thrall BD, Pounds JG, Teeguarden JG. A computational model of particle sedimentation, diffusion and target cell dosimetry for in vitro toxicity studies. Part Fibre Toxicol. 2010;7:36.
36. Huang Y, Cao J, Li X, Yang Q, Xie Q, Liu X, Cai X, Chen J, Hong H, Li R. Multimodal Feature Fusion Machine Learning for Predicting Chronic Injury Induced by Engineered Nanomaterials. [Unpublished manuscript].
37. Ashcroft T, Simpson JM, Timbrell V. Simple method of estimating severity of pulmonary fibrosis on a numerical scale. J Clin Pathol. 1988;41(4):467–70.
38. Strak M, Janssen NAH, Godri KJ, Gosens I, Mudway IS, Cassee FR, Lebret E, Kelly FJ, Harrison RM, Brunekreef B, Steenhof M, Hoek G. Respiratory Health Effects of Airborne Particulate Matter: The Role of Particle Size, Composition, and Oxidative Potential—The RAPTES Project. Environ Health Perspect. 2012;120:1183–9.
39. Tahara M, Fujino Y, Yamasaki K, Oda K, Kido T, Sakamoto N, Kawanami T, Kataoka K, Egashira R, Hashisako M, Suzuki Y, Fujisawa T, Mukae H, Suda T, Yatera K. Exposure to PM2.5 is a risk factor for acute exacerbation of surgically diagnosed idiopathic pulmonary fibrosis: a case–control study. Respir Res. 2021;22:80.
40. Vinikoor-Imler LC, Davis JA, Luben TJ. An Ecologic Analysis of County-Level PM2.5 Concentrations and Lung Cancer Incidence and Mortality. Int J Environ Res Public Health. 2011;8(6):1865–71.
41. Cui P, Huang Y, Han J, Song F, Chen K. Ambient particulate matter and lung cancer incidence and mortality: a meta-analysis of prospective studies. Eur J Public Health. 2015;25(2):324–9.
42. Cai XM, Dong J, Liu J, Zheng HZ, Kaweeteerawat C, Wang FJ, Ji ZX, Li RB. Multi-hierarchical profiling the structure-activity relationships of engineered nanomaterials at nano-bio interfaces. Nat Commun. 2018;9:4416.
43. Nel AE, Mädler L, Velegol D, Xia T, Hoek EMV, Somasundaran P, Klaessig F, Castranova V, Thompson M. Understanding biophysicochemical interactions at the nano-bio interface. Nat Mater. 2009;8(7):543–57.
44. Aminabad NS, Farshbaf M, Akbarzadeh A. Recent Advances of Gold Nanoparticles in Biomedical Applications: State of the Art. Cell Biochem Biophys. 2019;77(2):123–37.
45. Cho WS, Duffin R, Howie SEM, Scotton CJ, Wallace WAH, MacNee W, Bradley M, Megson IL, Donaldson K. Progressive severe lung injury by zinc oxide nanoparticles; the role of Zn^{2+} dissolution inside lysosomes. Part Fibre Toxicol. 2011;8:27.
46. Zhang J, Qin X, Wang B, Xu G, Qin ZX, Wang J, Wu LX, Ju XW, Bose DD, Qiu F, Zhou HH, Zou Z. Zinc oxide nanoparticles harness autophagy to induce cell death in lung epithelial cells. Cell Death Dis. 2017;8:e2954.
47. Li RB, Guiney LM, Chang CH, Mansukhani ND, Ji ZX, Wang X, Liao YP, Jiang W, Sun BB, Hersam MC, Nel AE, Xia T. Surface Oxidation of Graphene Oxide Determines Membrane Damage, Lipid Peroxidation, and Cytotoxicity in Macrophages in a Pulmonary Toxicity Model. ACS Nano. 2018;12(2):1390–402.
48. Liu X, Li JK, Zitolo A, Gao M, Jiang J, Geng XT, Xie QQ, Wu D, Zheng HZ, Cai XM, Lu JM, Jaouen F, Li RB. Doped Graphene To Mimic the Bacterial NADH Oxidase for One- Step NAD plus Supplementation in Mammals. J Am Chem Soc. 2023;145(5):3108–20.

49. Li RB, Ji ZX, Dong JY, Chang CH, Wang X, Sun BB, Wang MY, Liao YP, Zink JI, Nel AE, Xia T. Enhancing the Imaging and Biosafety of Upconversion Nanoparticles through Phosphonate Coating. ACS Nano. 2015;9(3):3293–306.
50. Schweiger C, Hartmann R, Zhang F, Parak WJ, Kissel TH, Rivera Gil P. Quantification of the internalization patterns of superparamagnetic iron oxide nanoparticles with opposite charge. J Nanobiotechnol. 2012;10:28.
51. Xu S, Zheng H, Ma R, Wu D, Pan Y, Yin C, et al. Vacancies on 2D transition metal dichalcogenides elicit ferroptotic cell death. Nat Commun. 2020;11:3484.
52. Présumé M, Simon-Deckers A, Tomkiewicz-Raulet C, Le Grand B, Van Tran J, Beaune G, et al. Exposure to metal oxide nanoparticles administered at occupationally relevant doses induces pulmonary effects in mice. Nanotoxicology. 2016;10(10):1535–44.
53. Wang X, Xia T, Ntim SA, Ji Z, George S, Meng H, et al. Quantitative Techniques for Assessing and Controlling the Dispersion and Biological Effects of Multiwalled Carbon Nanotubes in Mammalian Tissue Culture Cells. ACS Nano. 2010;4(12):7241–52.
54. Allen TJ, Spiteri AM. Growth factors in idiopathic pulmonary fibrosis: relative roles. Resp Res. 2001;3:13.
55. Ma Y, Guo Y, Ye YS, Huang HL, Lv KQ, Ke ZQ. Different effects of titanium dioxide nanoparticles instillation in young and adult mice on DNA methylation related with lung inflammation and fibrosis.Ecotox. Environ Safe. 2019;176:1–10.
56. Lardot CG, Huaux FA, Broeckaert FR, Declerck PJ, Delos M, Fubini B, Lison DF. Role of urokinase in the fibrogenic response of the lung to mineral particles. Amer. Thorac Soc. 1998;157(2):617–28.
57. Swennen B, Buchet JP, Stanescu D, Lison D, Lauwerys. R.,Epidemiologic survey of workers exposed to cobalt oxides, cobalt salts and cobalt metal. Br J Ind Med. 1993;50(9):835–42.
58. Badding MA, Fix NR, Orandle MS, Barger MW, Dunnick KM, Cummings KJ, Leonard SS. Pulmonary toxicity of indium-tin oxide production facility particles in rats. J Appl Toxicol. 2016;36(4):618–26.
59. Chang XH, Zhu A, Liu FF, Zou LY, Su L, Liu SK, Zhou HH, Sun YY, Han AJ, Sun YF, Li S, Li J, Sun YB. Nickel oxide nanoparticles induced pulmonary fibrosis via TGF-1 activation in rats. Hum Exp Toxicol. 2017;36(8):802–12.
60. Nweton PE, Bolte HF, Daly IW, Pillsbury BD, Terrill JB, Drew RT, Bendyke R, Sheldon AW, Rubin LF. Subchronic and chronic inhalation toxicity of antimony trioxide in the rat. Fundam Appl Toxicol. 1994;22(4):561–76.
61. Zhu MT, Nie GJ, Meng H, Xia T, Nel A, Zhao YL. Physicochemical Properties Determine Nanomaterial Cellular Uptake, Transport, and Fate. Acc Chem Res. 2013;46(3):622–31.
62. Liu Y, Workalemahu B, Jiang XY. The Effects of Physicochemical Properties of Nanomaterials on Their Cellular Uptake In Vitro and In Vivo. Small, 13 (43),1701815.
63. Li RB, Wang X, Ji ZX, Sun BB, Zhang HY, Chang CH, Lin SJ, Meng H, Liao YP, Wang MY, Li ZX, Hwang AA, Song TB, Xu R, Yang Y, Zink JI, Nel AE, Xia T. Surface Charge and Cellular Processing of Covalently Functionalized Multiwall Carbon Nanotubes Determine Pulmonary Toxicity. ACS Nano. 2013;7(3):2352–68.
64. Wang X, Ji ZX, Chang CH, Zhang HY, Wang MY, Liao YP, Lin SJ, Meng H, Li RB, Sun BB, Winkle LV, Pinkerton KE, Zink JI, Xia T, Nel AE. Use of Coated Silver Nanoparticles to Understand the Relationship of Particle Dissolution and Bioavailability to Cell and Lung Toxicological Potential. Small. 2013;10(2):385–98.
65. Calutu IM, Smarandescu RA, Rascu A. Biomonitoring Exposure and Early Diagnosis in Silicosis: A Comprehensive Review of the Current Literature. Biomedicines. 2023;11(1):100.
66. Rimal B, Greenberg AK, Rom WN. Basic pathogenetic mechanisms in silicosis: current understanding. Curr Opin Pulm Med. 2005;11(2):169–73.
67. Li RB, Ji ZX, Chang CH, Dunphy DR, Cai XM, Meng H, Zhang HY, Sun BB, Wang X, Dong JY, Lin SJ, Wang MY, Liao YP, Brinker CJ, Nel A, Xia T. Surface Interactions with Compartmentalized Cellular Phosphates Explain Rare Earth Oxide Nanoparticle Hazard and Provide Opportunities for Safer Design. ACS Nano. 2014;8(2):1771–83.
68. Bhattacharya M, Ramachandran P. Immunology of human fibrosis. Nat Immunol. 2023;24:1423–33.
69. Kolb M, Margetts PJ, Anthony DC, Pitossi F, Gauldie J. Transient expression of IL-1β induces acute lung injury and chronic repair leading to pulmonary fibrosis. J Clin Invest. 2001;107(12):1529–36.
70. Jain A, Irizarry-Caro RA, McDaniel MM, Chawla AS, Carroll KR, Overcast GR, Philip NH, Oberst A, Chervonsky AV, Katz JD, Pasare C. T cells instruct myeloid cells to produce inflammasome-independent IL-1β and cause autoimmunity. Nat Immunol. 2020;21(1):65–74.
71. Wang HR, Wu J, Ma L, Bai YF, Liu J. The role of interleukin-1 family in fibrotic diseases. Cytokine. 2023;165:156161.
72. Henderson NC, Rieder F, Wynn TA. Fibrosis: from mechanisms to medicines. Nature. 2020;587(7835):555–66.
73. Konduru NV, Murdaugh KM, Sotiriou GA, Donaghey TC, Demokritou P, Brain JD, Molina RM. Bioavailability, distribution and clearance of tracheally-instilled and gavaged uncoated or silica-coated zinc oxide nanoparticles. Part Fibre Toxicol. 2014;11:44.
74. Konduru NV, Molina RM, Swami A, Damiani F, Pyrgiotakis G, Lin P, Andreozzi P, Donaghey TC, Demokritou P, Krol S, Kreyling W, Brain JD. Protein corona: implications for nanoparticle interactions with pulmonary cells. Part Fibre Toxicol. 2017;14:42.
75. Sager TM, Kommineni C, Castranova V. Pulmonary response to intratracheal instillation of ultrafine versus fine titanium dioxide: role of particle surface area. Part Fibre Toxicol. 2008;5:17.
76. Vooght VD, Vanoirbeek JAJ, Haenen S, Verbeken E, Nemery B, Peter HM, Hoet PHM. Oropharyngeal aspiration: An alternative route for challenging in a mouse model of chemical-induced asthma. Toxicology. 2009, 259 (1–2), 84 – 9.
77. Porter DW, Hubbs AF, Mercer RR, Wu N, Wolfarth MG, Sriram K, Leonard S, Battelli L, Schwegler-Berry D, Friend S, Andrew M, Chen BT, Tsuruoka S, Endo M, Castranova V. Mouse pulmonary dose- and time course-responses induced by exposure to multi-walled carbon nanotubes. Toxicology. 2010;10(269):136–47.
78. Antonini JM, Badding MA, Meighan TG, Keane M, Leonard SS, Roberts JR. Evaluation of the pulmonary toxicity of a fume generated from a nickel-, copper-based electrode to be used as a substitute in stainless steel welding. Environ Health Insights. 2014;8(Suppl 1):11–20.
79. NIOSH. Appendix G. 1989 Air contaminants update project–exposure limits NOT in effect. 2015. http://www.cdc.gov/niosh/npg/nengapdxg.html. (accessed 11/25/2024).

Publisher's note